aerospace

MDPI

Article

Reducing Antenna Leakage in Quasi-Monostatic Satellite Radar Using Planar Metamaterials

Mohammad Reza Khalvati and Dominique Bovey *

Institute of Information and Communication Technologies, University of Applied Sciences of Western Switzerland (HEIG-VD/HES-SO), 1401 Yverdon-les-Bains, Vaud, Switzerland; mohammad.khalvati@heig-vd.ch
* Correspondence: dominique.bovey@heig-vd.ch

Abstract: In an autonomous robotic space debris removal mission, an essential sensor used for navigation is an FMCW radar designed for close-range relative navigation. To achieve the required range performance, minimizing RF leakage between the transmitter (Tx) and receiver (Rx) antennas is essential for the accurate detection of the range and velocity of the targeted space debris. Antennas positioned above the metallic satellite front face are highly susceptible to RF leakage, primarily caused by surface current propagation and lateral waves traveling parallel to the platform. This study presents two lightweight, single-layer planar metamaterials—a novel compact electromagnetic bandgap (EBG) and a non-uniform high-impedance surface (HIS)—optimized to suppress both surface waves and interact with space waves within the 9.3–9.8 GHz frequency range. These designs address strict size, weight, and power (SWaP) constraints while ensuring compatibility with extreme space conditions and resistance to mechanical shocks. Experimental validation indicates that a minimum Tx/Rx isolation improvement of 10 dB is achieved using the HIS, and 20 dB is achieved using the EBG across the radar's operational bandwidth (5%).

Keywords: antenna decoupling; planar metamaterials; antenna isolation; lateral wave suppression; electromagnetic bandgap; high-impedance surface; autonomous relative navigation

Citation: Khalvati, M.R.; Bovey, D. Reducing Antenna Leakage in Quasi-Monostatic Satellite Radar Using Planar Metamaterials. *Aerospace* **2024**, *11*, 1037. https://doi.org/10.3390/aerospace11121037

Academic Editor: Yan (Rockee) Zhang

Received: 5 November 2024
Revised: 10 December 2024
Accepted: 13 December 2024
Published: 19 December 2024

1. Introduction

In FMCW radar systems, mutual coupling or leakage between the Tx and Rx antennas introduces a false echo at zero range, limiting receiver sensitivity and reducing long-range detection performance [1,2]. This diminishes the signal-to-noise ratio (SNR) and reduces the maximum detectable range. Moreover, leaked Tx phase noise degrades detection performance for space debris with low relative velocities (a few m/s). In such scenarios, the low-frequency Doppler component (a few Hz) is masked by the phase noise, necessitating longer frequency sweeps, which increase energy consumption and demand greater DSP power and memory for signal processing [3,4].

Addressing Tx/Rx interference is a critical challenge for the ranging radar system in the ClearSpace Active Debris Removal mission [5]. In this mission, the antennas are separated by several tens of wavelengths and mounted on metallic satellite platforms. Leakage suppression is essential to prevent the formation of surface currents on the metallic platform and their propagation toward the receiver. Additionally, the system must interact with incident space waves, which impinge at various angles (parallel, oblique, and normal). The effective attenuation of interference is required across the radar's 5% bandwidth. The radar operates in the X-band with a central chirp frequency of 9.5 GHz.

Various techniques have been proposed to improve Tx/Rx isolation. For instance, enclosing antennas with 50 mm baffles has been shown to enhance isolation by up to 10 dB in the frequency range of 9.3–9.4 GHz [6]. Another approach involves using wave-absorbing materials, with their placement optimized through electromagnetic field analysis methods, such as generalized impedance density theory and Poynting vector methods [7].

However, these physical isolation methods are often unsuitable for space applications due to size and weight requirements and compatibility with the space environment. Wave absorbers may degrade under extreme temperatures [8], fail under radiation exposure, out-gas in a vacuum, risking the contamination of sensitive satellite components [9].

Active cancellation techniques, widely employed in FMCW radars, provide another solution by introducing additional hardware to suppress coupling between antennas [10,11]. However, canceling multiple path lengths requires multiple cancellation channels, increasing system size, weight, and power (SWaP) requirements and costs, making this approach impractical for many satellite applications.

Metamaterials (MMs) offer a promising alternative solution to improve Tx/Rx isolation. MMs can be categorized into planar (2D) and non-planar (3D) structures. While non-planar MMs, such as multilayered designs [12], corrugated surfaces [13], and pyramidal structures [14], offer wideband suppression, they are generally unsuitable for space applications due to their complexity and size, weight, and power (SWaP) constraints. Conversely, planar MMs, fabricated using PCB technology, are lightweight, reliable, and well suited for space applications.

Planar MMs have been extensively employed in applications such as improving the isolation of antennas in single-board radar systems [15] and planar MIMO systems [16–18]. In these applications, the primary focus of the design is to suppress slow-wave propagation, which is the dominant leakage mechanism in conventional systems. For instance, in [15], planar electromagnetic bandgap (EBG) structures were used to enhance isolation in FMCW radar systems (57–64 GHz) with Tx/Rx fabricated on the same substrate with separations of 3λ.

Another application of MMs is radar cross-section (RCS) reduction, where the goal is to attenuate waves striking the surface at normal or oblique angles [19,20]. In such cases, the structure was designed to reflect waves with an inverse phase, effectively canceling the incident waves.

A limitation of conventional planar metamaterial (MM) designs, such as electromagnetic bandgap (EBG) structures, is that the energy stored within the structure partially dissipates through ohmic losses, while a significant portion propagates along the cells. When this propagating energy encounters border cells, it may be either reflected back or re-radiated. The re-radiated energy can then propagate and be absorbed by the receiver antenna, leading to decreased isolation. In [21], a circuit-based nonlinear metasurface absorber is proposed to effectively suppress leakage in such scenarios for high-power applications. In this concept, MMs are designed with a series of rectification diodes to attenuate the RF energy stored within the MMs. Furthermore, in this research, as the antennas are positioned slightly above the platform, leakage can also occur in the form of lateral waves propagating parallel to the metallic platform. So, the optimized design must engage with all sorts of leakage.

This research addresses these limitations by proposing two planar metamaterial-based solutions optimized to suppress slow-wave propagation and re-direct radiated energy normal to the surface. A novel compact EBG design with a cell length of 3 mm and a non-uniform high-impedance surface (HIS) array are introduced to improve isolation between 9.3–9.8 GHz. The design procedures for both MMs are explained in detail. As mentioned, these solutions are specifically tailored to meet the unique challenges of the ClearSpace mission, providing enhanced Tx/Rx isolation. Measurement results confirm the effectiveness of these designs in improving isolation, highlighting their potential for satellite radar applications.

2. Design Wideband Meta-Materials for Antenna Decoupling

As mentioned earlier, the metallic plate beneath the Tx/Rx antenna supports wave propagation by inducing surface currents on the metallic platform. At the edge of the patch antenna, the surface wave in the antenna's substrate re-radiates, and a portion of this radiated energy propagates as a bounded wave toward the receiver. This bounded wave

is re-scattered when encountering discontinuities or surface textures along its path. As a result, the bounded wave reaches the Rx antenna and enters the receiver [22]. In addition, a portion of the radiated energy leaks directly into space as lateral wave propagation, which needs to be attenuated. Therefore, the MM should be designed to interact with lateral space waves, re-radiating or redirecting them away to prevent interference with the receiver.

Two distinct metasurfaces, high-impedance surface (HIS) and electromagnetic bandgap (EBG) structures, have been designed to effectively reduce leakage between the Tx and Rx patch antennas. In this study, the Tx and Rx antennas were positioned on a metallic surface with a fixed separation distance of 800 mm, representing the antenna placement on the metallic side of the satellite cube in the primary design of ClearSpace. Both antennas were mounted 16 mm above the metallic surface (Figure 1). The antennas used in this research were rectangular inset-fed patch antennas with a 9 dBi gain, resonating at 9.5 GHz. They were fabricated on a grounded RT Duroid 5870 substrate with a height of 1.57 mm. The dimensions of the patch antenna, as well as the simulated reflection and elevation cuts of its radiation pattern at azimuthal angles $\phi = 0^\circ$ and $\phi = 90^\circ$, are shown in Figure 2. In the polar plot, θ represents the polar angles measured with respect to the z-axis.

The primary objective was to improve the isolation level by about 20 dB, with respect to the reference without absorbers or MMs, across the entire operational frequency bandwidth of the FMCW radar, spanning from 9.3 GHz to 9.8 GHz. All the metasurfaces have been designed using a full-wave RF solver, HFSS (High-Frequency Structure Simulator) [23]. The ClearSpace FMCW radar systems use directional antennas with a much higher gain of the order of 20 dBi and a lower level of lateral radiation compared to the patch antennas. So, the worst-case scenario was studied in this research.

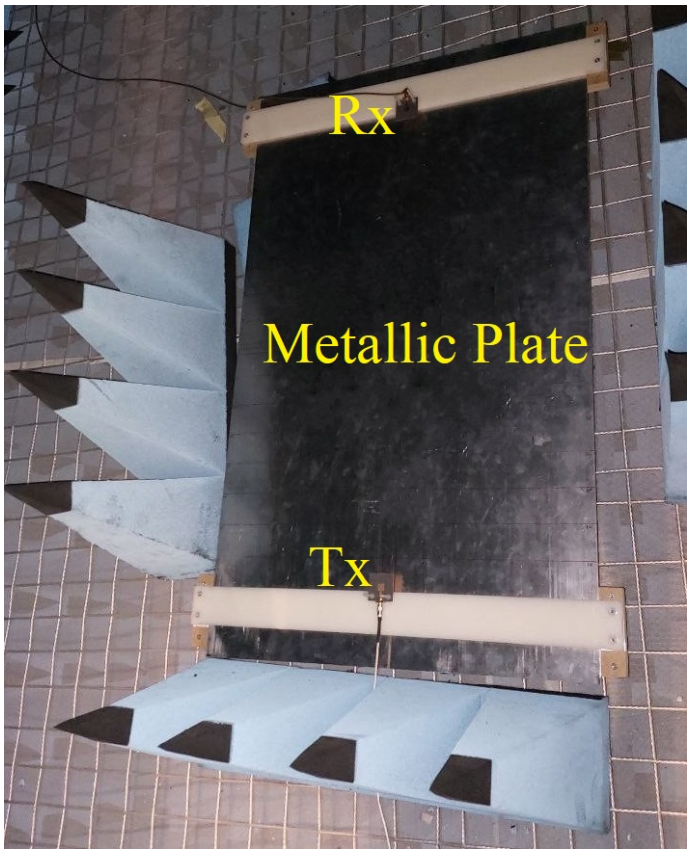

Figure 1. The simulated platform consists of two rectangular patch antennas mounted 16 mm above a large metallic plate.

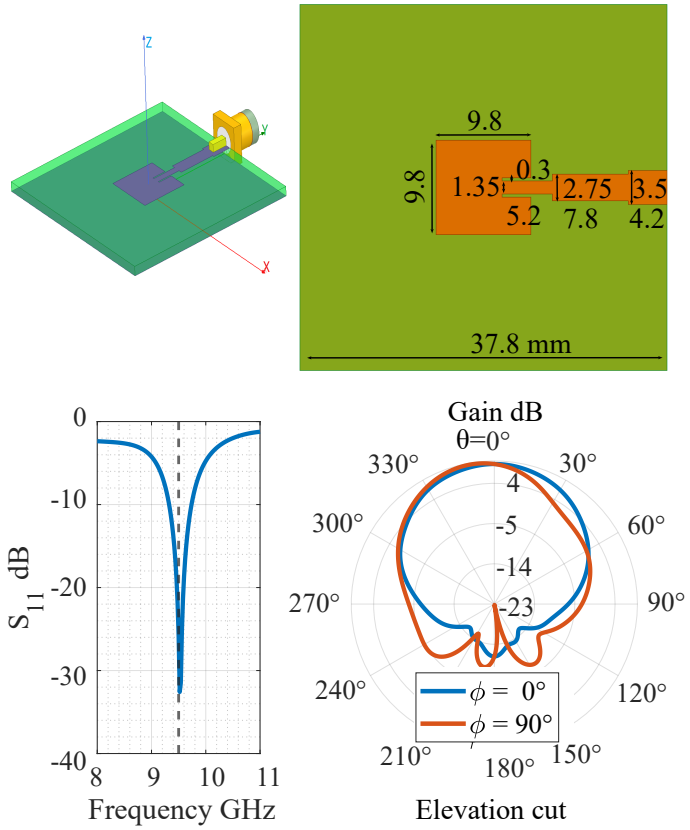

Figure 2. Top panel: 3D model and dimensions of the rectangular inset-fed patch antenna. Bottom left: reflection. Bottom right: elevation cuts of the radiation pattern at azimuthal angles $\phi = 0°$ and $\phi = 90°$.

2.1. Compact EBG Design

EBG structures are usually designed to provide a bandgap within a designated frequency range, effectively reducing the surface wave propagation of both TM and TE modes. As is mentioned, such a design is particularly advantageous in scenarios where antennas and metasurfaces are integrated on the same substrate, like MIMO or phased array antennas.

In our case, as antennas are situated above a metallic plate, the designed EBG must engage with space waves in addition to the surface wave, to maximize the isolation. Hence, the EBG structure needs to be designed to interact with space waves in the fast-wave leaky TE mode region [22].

A multi-objective genetic algorithm (MOGA) was applied to enhance the isolation capability of the EBG structure. The algorithm was implemented in MATLAB and integrated with HFSS [23] for electromagnetic simulations. The optimization process started with a randomly generated population, where each individual represented a candidate design for the EBG unit cell. The optimization targeted two key objectives: (1) attenuating slow-wave propagation along the metallic interface and (2) supporting radiative TE-waves within the frequency range of 9.3–9.8 GHz. These objectives were evaluated using the dispersion diagram obtained from eigenvalue simulations in HFSS. The theory behind the dispersion diagram and the methodology for analyzing its results are explained in the following paragraphs. The MOGA employed tournament selection with 20% of the population chosen for reproduction in each generation. Genetic operators, such as crossover and mutation, were used to explore the design space effectively. The optimization iterated over multiple generations until the algorithm converged, meeting the predefined fitness criteria for both objectives.

The efficiency of EBG in achieving these goals has been studied by analyzing the dispersion diagram. The dispersion diagram illustrates how surface waves propagate through infinite 2D periodic EBG structures, identifying the frequency ranges where wave propagation is permitted or prohibited. An eigenmode full-wave EM solver was utilized to extract the dispersion diagram. The periodic boundary condition was applied to the unit cell borders. All four branches in the patch are identical and have rotational symmetry with respect to the center of the cell.

The dispersion diagram of the optimized EBG are shown in Figure 3. In the dispersion curve, the supported frequencies are calculated as a function of wave-number k along the symmetry points in the reciprocal space, called the Brillouin zone. For a unit cell with rotational symmetry, it is enough to calculate the $\omega(k)$ inside the smaller triangular area known as the irreducible Brillouin zone (Figure 3). The dispersion curve is calculated along the line connecting these high-symmetry points. For a square lattice with the length of a, the symmetry points are marked with Γ(k = (0,0)), X (k = (π/a,0)), and M (k = (π/a,π/a)) [24].

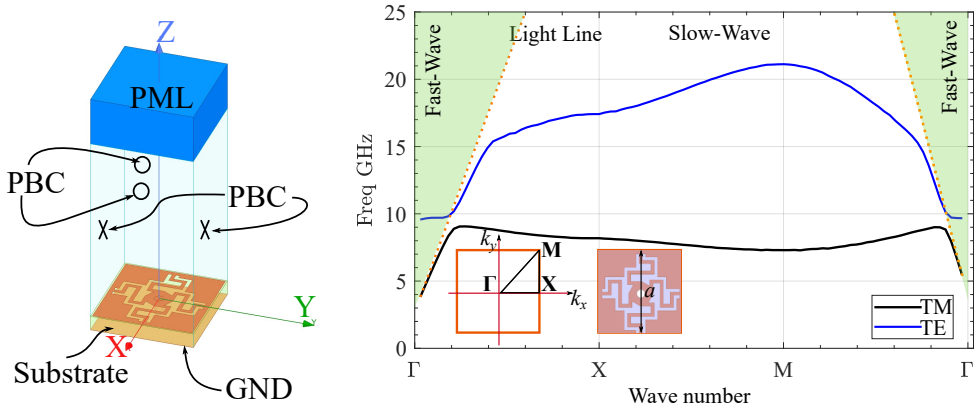

Figure 3. (**Left**): The EM model of a unit compact EBG cell. (**Right**): The dispersion curve of the optimized EBG structure demonstrates its ability to suppress slow waves within the operational frequency band and re-radiate electromagnetic energy as a leaky TE mode between 9.3 and 9.8 GHz.

The TM band starts at DC ($k_x, k_y \rightarrow 0$) and consistently remains within the slow-wave region, positioned below the light line, indicating bounded surface wave propagation. In contrast, in the Γ-X direction, the TE band starts in the fast-wave region, highlighted in green in Figure 3. The supported wave in this region has the phase velocity v_{ph} higher than the speed of light. These waves are referred to as TE leaky modes because they possess radiative characteristics and can couple with space waves [22,25]. So, in the frequency ranges of 9.3 to 9.8 GHz, the EBG structure can interact with lateral waves and re-radiate them as space waves perpendicular to the EBG plane.

As the wave vector k increases, the dispersion curve intersects the light line and continues with a phase velocity v_{ph} lower than the speed of light. In the slow-wave region, a bandgap is created, which means the slow-wave propagation in the entire FMCW operational bandwidth is not supported, and slow waves are attenuated. The same argument applies to the third path, i.e., the M-Γ direction.

The dimensions of the designed EBG unit cell and the fabricated panel are illustrated in Figure 4. The unit cell is compact with dimensions of 3.35 mm × 3.35 mm. The EBG panel was fabricated on a 0.508 mm Roger 4350 substrate.

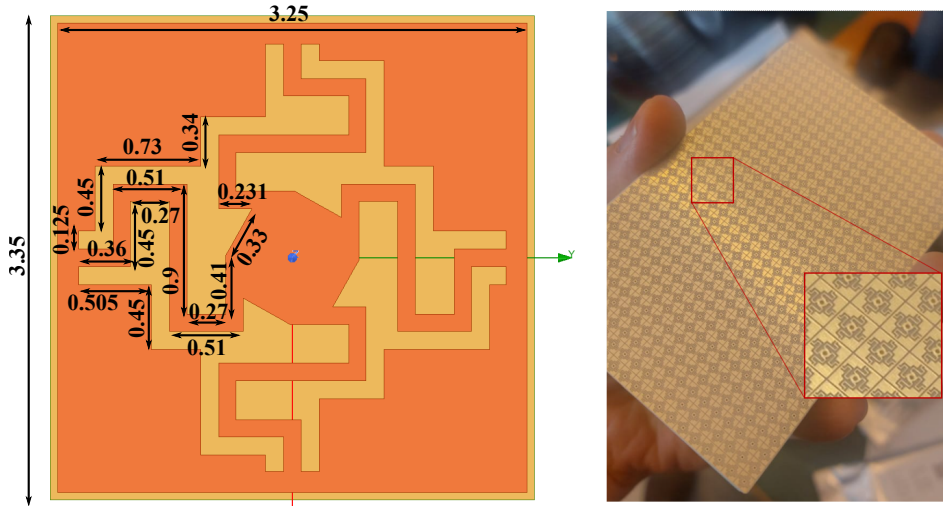

Figure 4. (**Left**): The optimized EBG unit cell. (**Right**): The EBG panel made with the optimized unit cell. Panel dimensions: 60 mm × 100 mm.

2.2. Broadband Textured HIS Design

HIS surfaces are a periodic arrangement of resonant elements designed to control surface wave propagation in a specific and predefined manner. These surfaces are created by texturing the interface between two media, by implementing an infinite array of 2D printed circuit elements including frequency-selective surfaces (FSSs) [26–28]. HIS surfaces are engineered to achieve specific impedance characteristics at a certain range of frequencies. When an incident wave approaches the HIS surface, it induces surface currents and electric charges on the interface so that the incident wave reflects in a specific spatial direction. In our research, the design of HIS aims to redirect the space waves far away from the receiver antenna.

In the design of the unit HIS cell, an infinite 2D periodic array of square patches on a grounded Roger 4350 substrate was first considered. A 3D full-wave EM model of a single cell was employed to extract the impedance of the HIS unit cell (Figure 5). The Floquet boundary condition was applied. Perfect Electric Conductors (PEC) were assigned to all metallic elements, and the thickness of the substrate was 0.508 mm. The impedance of HIS surface Z_{HIS}, can be extracted directly with

$$Z_{\text{HIS}} = \frac{\overline{E_x}}{\overline{H_y}}. \tag{1}$$

Here, $\overline{E_x}$ and $\overline{H_y}$ represent the average x component of the electric and y component of the magnetic fields at the interface [29–31]. The variation in Z_{HIS} as a function of gap sizes at four different frequencies is plotted in Figure 6. In all cases, the cell length is kept unchanged at 8.33 mm.

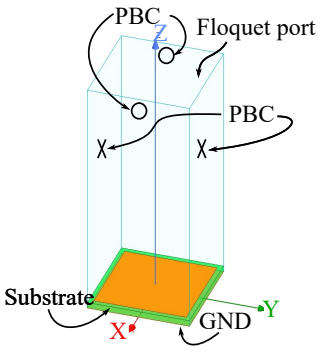

Figure 5. The electromagnetic model of the unit HIS cell used to calculate the impedance of the cell.

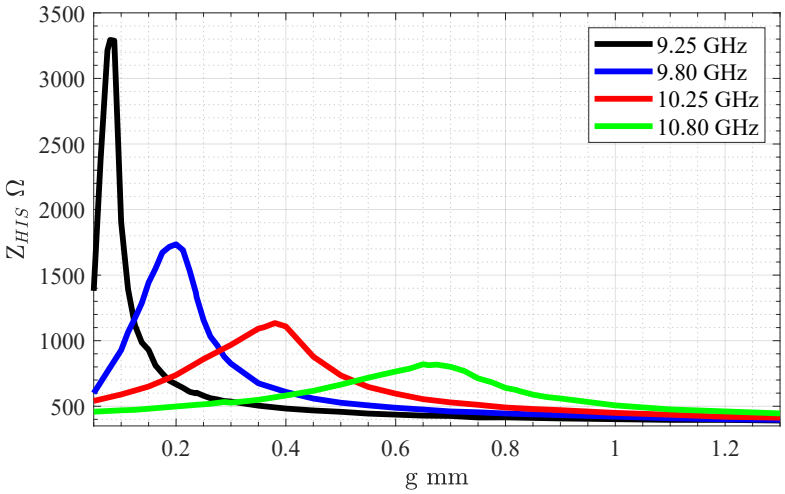

Figure 6. HIS impedance variation as a function of gap length at different frequencies.

To overcome the narrow bandwidth characteristic of a uniform gap length HIS, an array of non-uniform patches with varying gap lengths was designed. From Figure 6, it can be observed that the peak of Z_{HIS} shifts toward a larger gap length as the frequency increases. This implies the possibility of covering a wider frequency range with a varying gap length structure.

The design and optimization of the non-uniform HIS surface focuses on achieving minimum radiated power in a lateral direction using a 4 × 2 array of HIS macro-cells within the frequency range of 9.3 to 9.8 GHz (Figure 7). Each macro-cell has a two-fold symmetry around axes AA′ and BB′ (Figure 7: zoomed-in panel). A genetic algorithm optimization method was employed to minimize the elevation plan's far-field radiation of a patch antenna (YZ plane). The antenna is located 65 mm away from the non-uniform HIS panel shown in Figure 7. The ground layer is a PEC. The dimensions of the macro-cell and gap distances between the ith and jth patches, g_{ij}, are listed in Table 1.

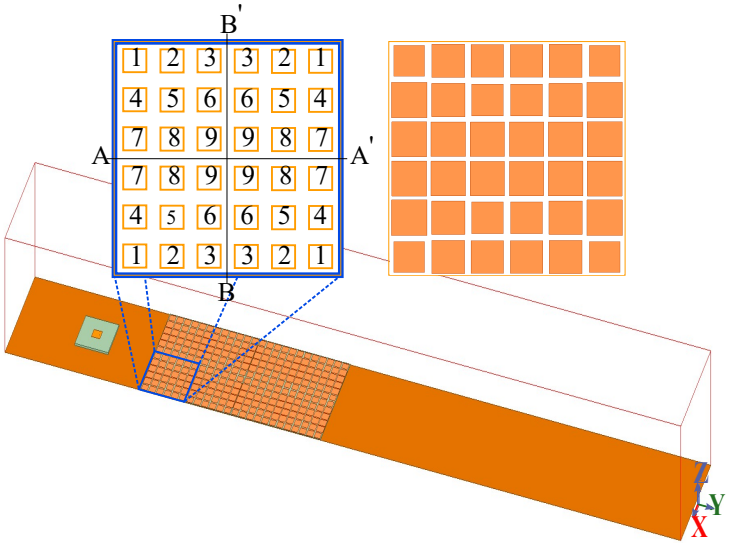

Figure 7. The simulation model used for optimizing the HIS surface and the arrangements of patches in each macro-cell. The objective is to minimize the lateral radiated energy in the YZ plane using an array of 4 × 2 macro-cells. The top right plot shows the optimized macro-cell.

The radiated far-field gain at different frequencies in the YZ plane is shown in Figure 8. As depicted in the figure, a minimum isolation of about 14 dB was achieved using a 2 × 4 macro-cell panel for all frequencies higher than 9.4 GHz. A photo of the fabricated HIS panel, which contains 4 × 6 macro-cells, is shown in Figure 9.

Table 1. Dimensions of optimized HIS macro-cell.

Param	mm	Param	mm	Param	mm
g_{12}	1.57	g_{23}	1.37	g_{45}	1.01
g_{56}	1.41	g_{78}	0.95	g_{89}	1.01
g_{14}	1.30	g_{47}	0.84	g_{25}	1.30
g_{58}	1.12	g_{36}	1.50	g_{69}	1.30
g_{11}	1.81	g_{22}	1.32	g_{33}	1.42
g_{66}	1.58	g_{99}	1.03	g_{77}	0.90
g_{88}	1.00	AA'	50.00	BB'	50.00

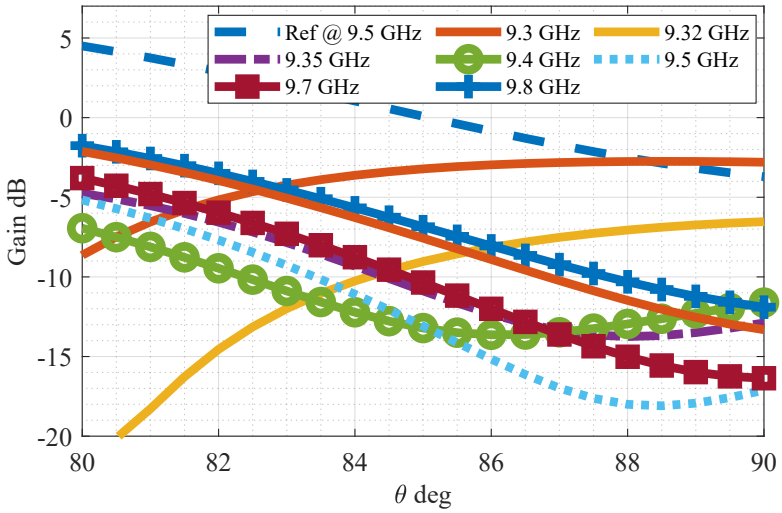

Figure 8. The radiated far-field gain at different frequencies in the YZ plane.

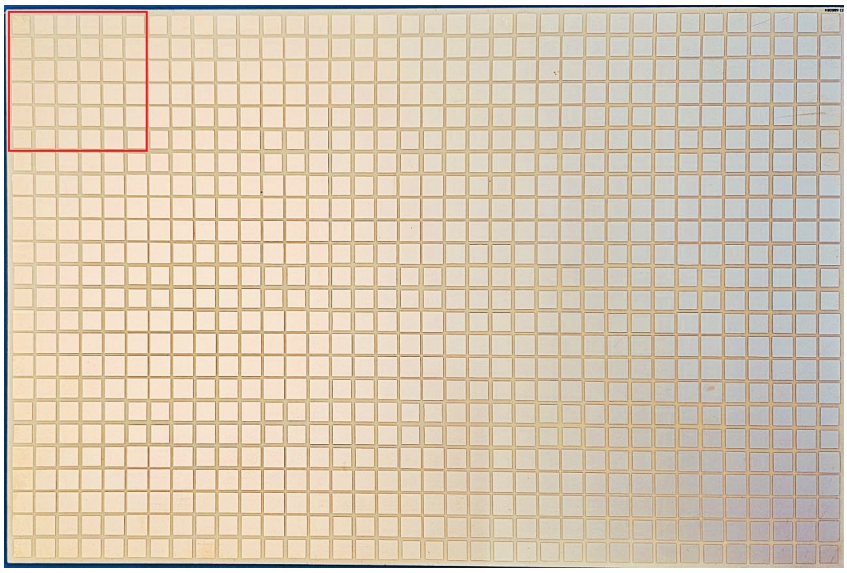

Figure 9. Fabricated HIS panel. The panel consists of 4 × 6 macro-cells. The red square represents a single HIS macro-cell.

3. Experimental Validation of HIS and EBG Structures

The efficiency of designed MMs in suppressing the mutual coupling of Tx/Rx patch antennas on a metallic ground plane was measured (Figure 10). As is mentioned, two identical patch antennas with the center resonance frequency of 9.5 GHz were located on opposing ends of a rectangular aluminum ground plate. Both antennas were mounted 16 mm above the metallic plate, and the distance between the two antennas was set to 800 mm.

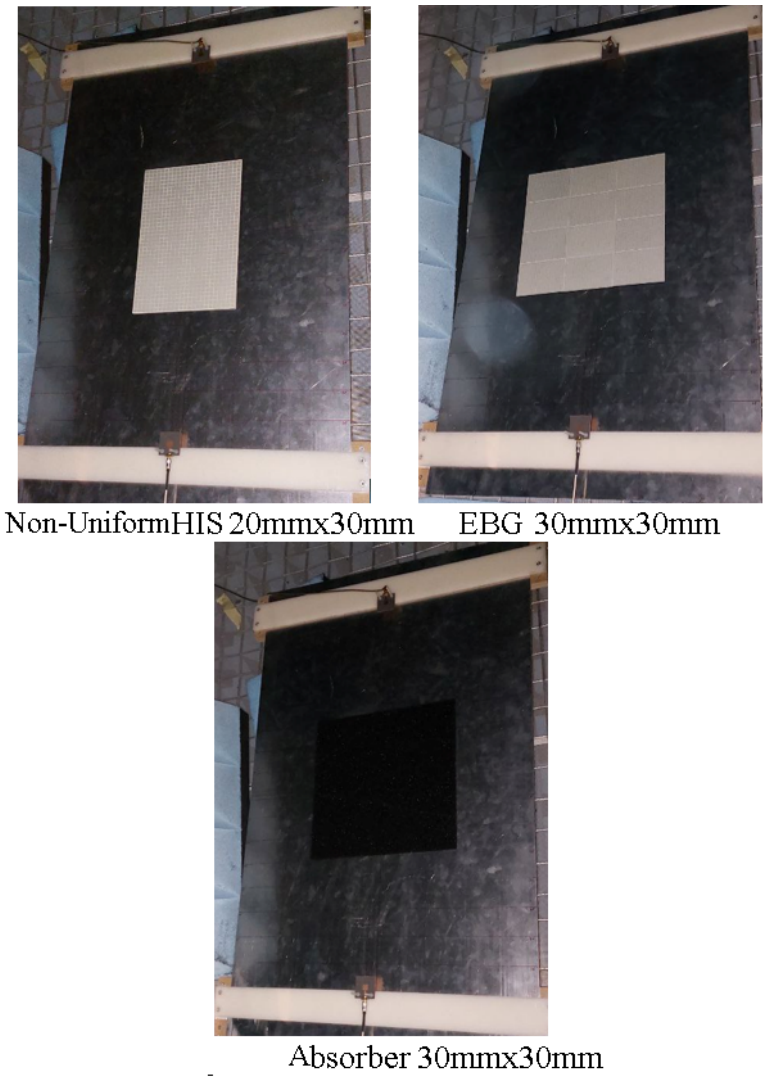

Figure 10. The measurement setup includes two patch antennas mounted on a metallic ground plate. Three different strategies for attenuating mutual coupling between the antennas were measured.

The coupling between two antennas S_{21} was measured in an anechoic chamber for different cases: with EBG blocks at the center, with an HIS sheet, and with an absorber sheet (Figure 10). The absorber sheet used in this measurement was Laird Eccosorb HR-10 with a frequency range between 5 and 90 GHz. The measured results are plotted in Figure 11 and compared with the reference measurement, which was taken without any absorber between the two antennas. The measurement results indicate that the designed EBG surface has a wider absorbing frequency range compared to HIS. A single HIS panel suppresses leakage starting from 9.4 GHz, and the EBG surface dissipates incident power from around 9.1 GHz. At higher frequencies up to 9.8 GHz, both HIS and EBG sheets reduce the coupling by about 10 dB as the absorber sheet does.

The coupling reduction between two antennas is measured when a larger area between the antennas is covered with MMs, as shown in Figure 12. The total coupling reduction for both cases is plotted in the same figure. HIS sheets dissipate surface waves at frequencies above 9.2 GHz. At 9.3 GHz, the isolation improves by approximately 10 dB, reaching 20 dB in the frequency range of 9.4–9.8 GHz. The EBG layers start operating at 8.5 GHz, providing an average isolation improvement of -20 dB between 9.1 and 9.8 GHz. At higher frequencies, the decoupling improvement remains significant, achieving about 10 dB at 10 GHz.

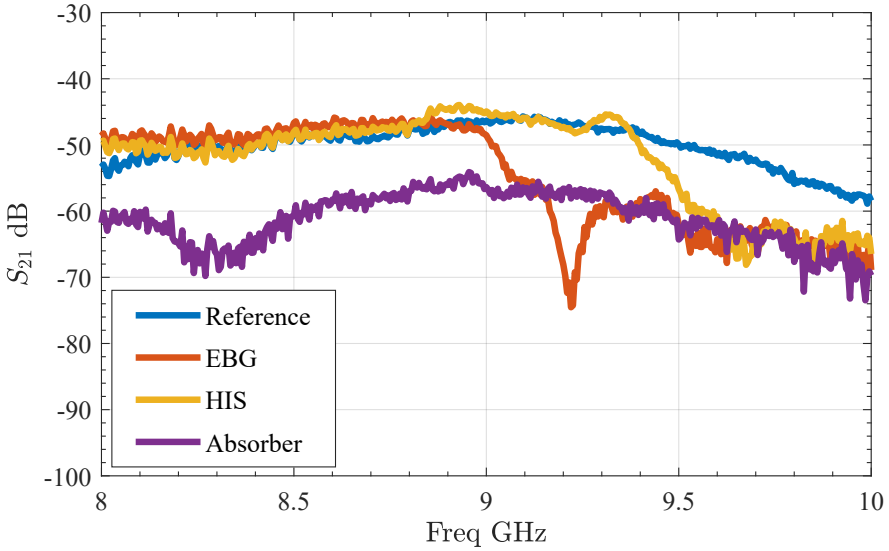

Figure 11. The measured coupling between antennas in the presence of HIS, EBG, and a conventional absorber.

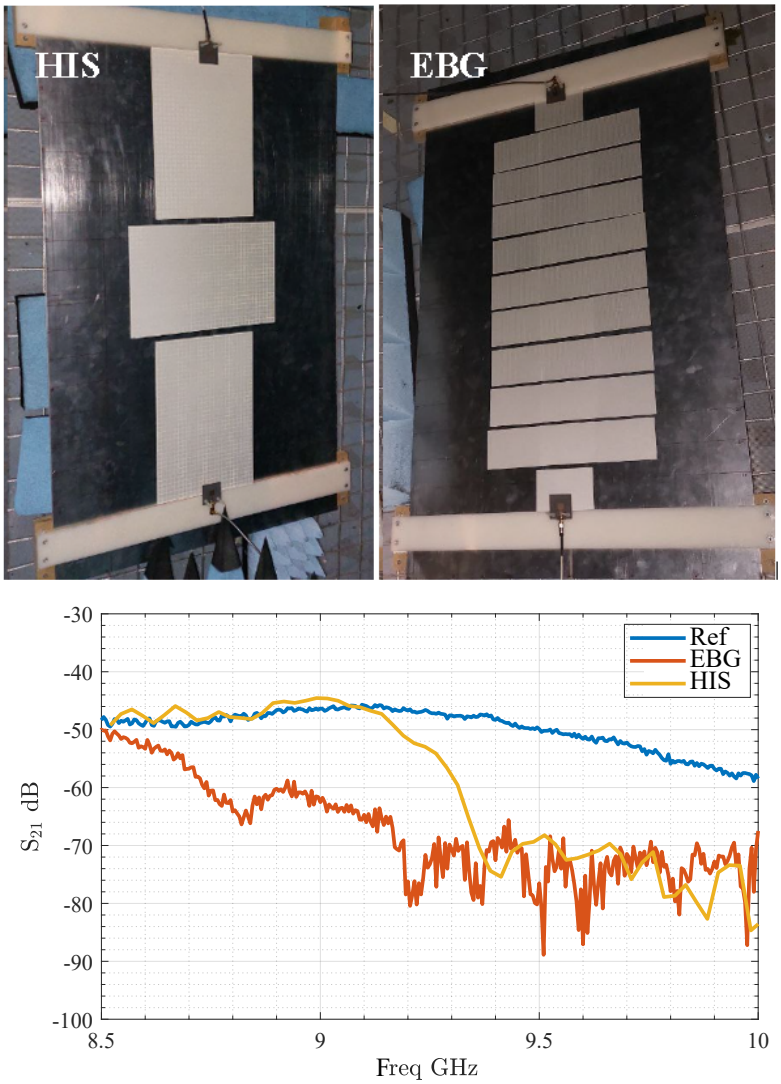

Figure 12. Antenna decoupling, when the space between two antennas is covered with MMs.

4. Conclusions

This study presented the design, optimization, and experimental validation of planar metamaterials—a novel compact EBG and non-uniform HIS structure—for enhancing Tx/Rx isolation in FMCW radar systems used in robotic space debris removal missions. The EBG design effectively suppressed both slow and fast waves, achieving isolation improvements of up to 20 dB within the operational bandwidth of 9.2–9.8 GHz, while the HIS structure redirected lateral waves, providing an isolation improvement of 10 dB at 9.3 GHz and a minimum of 20 dB at frequencies above 9.4 GHz. Experimental results confirmed the performance of these metasurfaces, demonstrating significant coupling suppression for both partial- and full-coverage scenarios. These designs meet stringent SWaP requirements and ensure robustness for space applications under extreme conditions.

Author Contributions: Conceptualization, M.R.K.; methodology, M.R.K.; software, M.R.K.; formal analysis, M.R.K.; investigation, M.R.K.; resources, M.R.K.; data curation, M.R.K.; writing—original draft preparation, M.R.K. and D.B.; writing—review and editing, M.R.K. and D.B.; visualization, M.R.K.; supervision, D.B.; project administration, D.B.; funding acquisition, D.B. All authors have read and agreed to the published version of the manuscript.

Funding: This work was conducted under the Innosuisse project "ARCOROSSO—Antennas for Radar Sensor and Communication for On-orbit Robotic Servicing Spacecraft and their Optimization", grant number 50551.1.

Data Availability Statement: The data presented in this study are available on request from the corresponding author.

Acknowledgments: The measurements were performed at the Microwave and Antenna Group (MAG) facility at the Swiss Federal Institute of Technology (EPFL), and the authors gratefully acknowledge the support and advice of Anja Skrivervik (EPFL-MAG) and her team.

Conflicts of Interest: The authors declare no conflicts of interest.

References

1. Aghighi, A.; Essawy, M.; Natarajan, A. A mm-wave FMCW radar RX frontend in CMOS with modulated self-interference cancellation path. In Proceedings of the 2022 IEEE 22nd Topical Meeting on Silicon Monolithic Integrated Circuits in RF Systems (SiRF), Las Vegas, NV, USA, 16–19 January 2022; pp. 13–15.
2. Phuoc, P.V.N.T.; Tang, L.; Mukhopadhyay, S.C.; Nguyen, D.M.; Hasan, F. Probabilities of false alarm for vital sign detection on the basis of a Doppler radar system. *Sensors* **2018**, *18*, 694. [CrossRef]
3. Beasley, P.D.L. The influence of transmitter phase noise on FMCW radar performance. In Proceedings of the 2006 European Microwave Conference, Manchester, UK, 10–15 September 2006; pp. 1810–1813.
4. Siddiq, K.; Watson, R.J.; Pennock, S.R.; Avery, P.; Poulton, R.; Dakin-Norris, B. Phase noise analysis in FMCW radar systems. In Proceedings of the 2015 European Microwave Conference (EuMC), Paris, France, 7–10 September 2015; pp. 1523–1526.
5. Biesbroek, R.; Aziz, S.; Wolahan, A.; Cipolla, S.; Richard-Noca, M.; Piguet, L. The clearspace-1 mission: ESA and clearspace team up to remove debris. In Proceedings of the 8th European Conference on Space Debris, Darmstadt, Germany, 20–23 April 2021; pp. 1–3.
6. Kuo, F.-Y.; Hwang, R.-B. High-isolation X-band marine radar antenna design. *IEEE Trans. Antennas Propag.* **2014**, *62*, 2331–2337.
7. Lundgren, J.; Malmström, J.; Hannula, J.-M.; Jonsson, B.L.G. Visualization and reduction of mutual coupling between antennas installed on a platform. *IEEE Trans. Electromagn. Compat.* **2021**, *64*, 92–101. [CrossRef]
8. Gao, C.; Jiang, Y.; Cai, D.; Xu, J.; Xiao, W. Effect of Temperature on the Microwave-Absorbing Properties of an Al_2O_3–$MoSi_2$ Coating Mixed with Copper. *Coatings* **2021**, *11*, 940. [CrossRef]
9. Coonrod, J. What Is Outgassing and When Does It Matter. Available online: https://www.example.com (accessed on 22 July 2010).
10. Zhang, J.; He, F.; Li, W.; Li, Y.; Wang, Q.; Ge, S.; Xing, J.; Liu, H.; Li, Y.; Meng, J. Self-interference cancellation: A comprehensive review from circuits and fields perspectives. *Electronics* **2022**, *11*, 172. [CrossRef]
11. Lu, H.; Huang, C.; Taranetz, M.; Schwarz, S.; Shao, S. Quadrature down-conversion based analog self-interference cancellation for continuous wave radars. In Proceedings of the 2016 IEEE Globecom Workshops (GC Wkshps), Washington, DC, USA, 4–8 December 2016; pp. 1–6.
12. Yu, P.; Besteiro, L.V.; Huang, Y.; Wu, J.; Fu, L.; Tan, H.H.; Jagadish, C.; Wiederrecht, G.P.; Govorov, A.O.; Wang, Z. Broadband metamaterial absorbers. *Adv. Opt. Mater.* **2019**, *7*, 1800995. [CrossRef]

13. Ren, J.; Yin, J.Y. 3D-printed low-cost dielectric-resonator-based ultra-broadband microwave absorber using carbon-loaded acrylonitrile butadiene styrene polymer. *Materials* **2018**, *11*, 1249. [CrossRef]
14. Lobet, M.; Lard, M.; Sarrazin, M.; Deparis, O.; Henrard, L. Plasmon hybridization in pyramidal metamaterials: A route towards ultra-broadband absorption. *Opt. Express* **2014**, *22*, 12678–12690. [CrossRef] [PubMed]
15. Adela, B.B.; van Beurden, M.C.; Zeijl, P.v.; Smolders, A.B. High-isolation array antenna integration for single-chip millimeter-wave FMCW radar. *IEEE Trans. Antennas Propag.* **2018**, *66*, 5214–5223. [CrossRef]
16. Al-Bawri, S.S.; Islam, M.T.; Islam, M.S.; Singh, M.J.; Alsaif, H. Massive metamaterial system-loaded MIMO antenna array for 5G base stations. *Sci. Rep.* **2022**, *12*, 14311. [CrossRef] [PubMed]
17. Iqbal, A.; Saraereh, O.A.; Bouazizi, A.; Basir, A. Metamaterial-based highly isolated MIMO antenna for portable wireless applications. *Electronics* **2018**, *7*, 267. [CrossRef]
18. Sokunbi, O.; Attia, H. Dual-layer dual-patch EBG structure for isolation enhancement and correlation reduction in MIMO antenna arrays. *Prog. Electromagn. Res. C* **2020**, *100*, 233–245. [CrossRef]
19. Liu, Q.; Chen, H.; Yan, Y.; Yao, X.; Liang, D.; Xie, J.; Deng, L. RCS reduction metasurface based on orbital angular momentum. *Results Phys.* **2023**, *53*, 107008. [CrossRef]
20. Chen, J.; Cheng, Q.; Zhao, J.; Dong, D.S.; Cui, T.J. Reduction of radar cross section based on a metasurface. *Prog. Electromagn. Res.* **2014**, *146*, 71–76. [CrossRef]
21. Wakatsuchi, H.; Kim, S.; Rushton, J.J.; Sievenpiper, D.F. Circuit-based nonlinear metasurface absorbers for high power surface currents. *Appl. Phys. Lett.* **2013**, *102*, 214103. [CrossRef]
22. Sievenpiper, D.; Zhang, L.; Broas, R.F.J.; Alexopolous, N.G.; Yablonovitch, E. High-impedance electromagnetic surfaces with a forbidden frequency band. *IEEE Trans. Microw. Theory Tech.* **1999**, *47*, 2059–2074. [CrossRef]
23. ANSYS, Inc. ANSYS HFSS. 2020. Available online: https://www.ansys.com/products/electronics/ansys-hfss (accessed on 4 November 2024).
24. Abegaonkar, M.; Kurra, L.; Koul, S.K. *Printed Resonant Periodic Structures and Their Applications*; CRC Press: Boca Raton, FL, USA, 2016.
25. Coulombe, M.; Koodiani, S.F.; Caloz, C. Compact elongated mushroom (EM)-EBG structure for enhancement of patch antenna array performances. *IEEE Trans. Antennas Propag.* **2010**, *58*, 1076–1086. [CrossRef]
26. Cai, B.G.; Li, Y.B.; Ma, H.F.; Jiang, W.X.; Cheng, Q.; Cui, T.J. Leaky-wave radiations by modulating surface impedance on subwavelength corrugated metal structures. *Sci. Rep.* **2016**, *64*, 2397. [CrossRef]
27. Asadpor, L.; Sharifi, G.; Rezvani, M. Design of a high-gain wideband antenna using double-layer metasurface. *Microw. Opt. Technol. Lett.* **2019**, *61*, 1004–1010. [CrossRef]
28. Joe, Y.S.; Essiben, J.F.D.; Cooney, E.M. Radiation characteristics of waveguide antennas located on the same impedance plane. *J. Phys. D Appl. Phys.* **2008**, *41*, 125503. [CrossRef]
29. Lee, J.; Sievenpiper, D.F. Method for extracting the effective tensor surface impedance function from nonuniform, anisotropic, conductive patterns. *IEEE Trans. Antennas Propag.* **2019**, *67*, 3171–3177. [CrossRef]
30. Hassani Gangaraj, S.A.; Monticone, F. Molding light with metasurfaces: From far-field to near-field interactions. *Nanophotonics* **2018**, *7*, 1025–1040. [CrossRef]
31. Homma, H.; Akram, M.R.; Fathnan, A.A.; Lee, J.; Christopoulos, C.; Wakatsuchi, H. Anisotropic impedance surfaces activated by incident waveform. *Nanophotonics* **2022**, *11*, 1989–2000. [CrossRef] [PubMed]